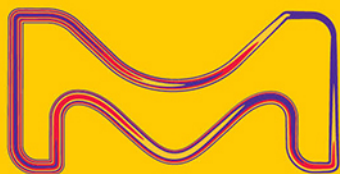# catch the SUN

Product Category list:
- Organic Photovoltaic (OPV) Donors and Acceptors
- Dye-Sensitized Solar Cell Materials
- Perovskite Materials

Visit us at:
SigmaAldrich.com/organic-electronics

MilliporeSigma is the U.S. and Canada Life Science business of Merck KGaA, Darmstadt, Germany.

Sigma-Aldrich®
Lab & Production Materials

Ultrasound Propagation in Lithium-Ion Battery Cell Materials: Basis for Developing Monitoring and Imaging Methods

Lukas Gold,* Thomas Herzog, Frank Schubert, Henning Heuer, and Guinevere A. Giffin*

State-of-the-art methods to monitor the degree of wetting of lithium-ion batteries during production, which are applicable at an industrial scale, are not capable of determining the spatial electrolyte distribution in the porous network of electrodes and separator. Ultrasound can bridge this gap as it has previously been proven to be a suitable method to monitor or evaluate the infiltration of porous structures, for example, epoxy resin in carbon fiber composite. Herein, the acoustic properties of different battery cell materials are evaluated over a wide frequency range in both the dry and wet states, for the first time. Furthermore, a collection of input parameters, from the experimental setup and the evaluation routine to the acoustic parameters of the battery materials themselves, are provided. These parameters are needed for the adaptation of ultrasonic nondestructive testing to the monitoring of the wetting process of a lithium-ion battery. Most importantly, this work demonstrates that a large change in the sound velocity (up to 100%) is observed when the porous structure of a lithium-ion battery is filled with electrolyte and thus can serve as an appropriate evaluation figure of merit.

L. Gold, G. A. Giffin
Fraunhofer R&D Center Electromobility
Fraunhofer Institute for Silicate Research ISC
97082 Würzburg, Germany
E-mail: lukas.gold@isc.fraunhofer.de; guinevere.giffin@isc.fraunhofer.de

T. Herzog, F. Schubert, H. Heuer
Department of Systems for Testing and Analysis
Fraunhofer Institute for Ceramic Technologies and Systems IKTS
01109 Dresden, Germany

H. Heuer
Institute of Electronic Packaging Technology
Technische Universität Dresden
01069 Dresden, Germany

G. A. Giffin
Chemical Technology of Materials Synthesis
Faculty of Chemistry and Pharmacy
Julius-Maximilians-University Würzburg
97070 Würzburg, Germany

1. Introduction

1.1. Electrolyte Filling and Wetting of Lithium-Ion Battery Cells

With a growing demand for cheap and reliable lithium-ion batteries, manufacturing processes are being optimized continuously to reduce energy consumption and costs. However, one of the main contributors to the manufacturing cost[1,2]—the wetting of the porous structure within the battery cell—still needs a gain in process knowledge to enable further acceleration and improvement.[3] After filling the battery cell with electrolyte, wetting is the next step in the process chain and involves a rest period under controlled conditions.[4,5] Unfortunately, there is uncertainty about the degree of wetting achieved and thus a safety margin is often used, which adds to the total time for this step.

The wetting process is usually performed at elevated temperatures and may, depending on cell geometry and type, even involve additional steps of electrolyte dosing. To ensure a high battery cell quality, reliable performance, and safety, the wetting has to be completed before the subsequent formation step is performed. Otherwise, a nonhomogeneous deposition of the initial solid–electrolyte interface (SEI) is expected,[4,6] causing an accelerated aging of the battery cells.[7–9] Therefore, best practice solutions are in place to ensure a sufficiently long wetting time. These solutions are based on experience with the production of battery cells with similar specifications and postmortem studies to visually inspect the wetting degree and the uniformity of the formation process. An in-line testing method to be able to test the wetting degree of each battery cell or to determine the best parameters for sufficient wetting of a battery cell type in preproduction development is highly desirable.[10] Such a method would enable the process time to be shortened to a minimum without the need for a safety margin.

1.2. Monitoring and Testing of the Wetting Process

There is currently no imaging or testing method, applicable on an industrial scale, able to spatially resolve the electrolyte distribution within a battery cell. Electrochemical impedance

ADVANCED
SCIENCE NEWS
www.advancedsciencenews.com

Energy Technology
Generation, Conversion, Storage, Distribution

www.entechnol.de

spectroscopy (EIS) is used to estimate the wetting degree,[11,12] The high-frequency resistance (HFR) is used as a measure for the wet electrode area, which is determined from the intersection in the Nyquist plot with the axis denoting the real part of the impedance, for example, where the imaginary part is zero, in the MHz–kHz frequency range. As the HFR is closely related to the ohmic resistance of the battery cell, which results from the electrical resistance of the cell components and the conductivity of the electrolyte,[11] its ability to measure the wetting of the microporous surface area of the electrodes is limited. The wetting of this surface is best measured by the charge transfer (CT) resistance, as its magnitude is inversely proportional to the wet, electrochemically active surface area. Unfortunately, the time required to measure the spectra in the low-frequency range (Hz–mHz), hosting the CT, renders EIS inadequate for the measurement of the microporous wetting.

Imaging methods such as infrared thermography,[11] X-ray,[10] and neutron radiography[2,5,7,12] or optical methods applied to battery cells with a transparent window[13] have been demonstrated to be feasible at the laboratory scale. The advancement of the wetting front within the battery cell as a whole was visualized in a number of reports,[5,10,12,13] but the degree of wetting of microporous structure could not be accessed. Ultrasound-based imaging methods might bridge this gap. The use of scanning ultrasound microscopy for the imaging of different types of lithium-ion battery cells has been demonstrated.[14,15] Pitta Bauermann et al. have shown that by applying different gates, for example, selecting different sections to discriminate the depth within the sample, to the ultrasonic signals returned in pulse-echo geometry, the resolution of the internal structure in different depths is possible.[14] Deng et al. demonstrated that in transmission geometry, ultrasound can be used to resolve the degree of wetting within a battery cell by evaluating the transmitted amplitude.[15] The latter method relies on the strong attenuation of ultrasound by the gas volume in its pathway. This means that gas bubbles and dry or "unwet" areas of the battery cell can be made visible by ultrasound.

1.3. Propagation of Ultrasound in Lithium-Ion Battery Cell Materials

The discussion on how to describe the propagation and attenuation of ultrasound in lithium-ion batteries and their constituents is ongoing. The applicable theories might vary depending on the measurement technique and probed frequency range. It was suggested that lithium-ion battery cells in an electrolyte-filled and functional state may be treated like an isotropic, elastic solid, if the wavelength λ of the compressional sound waves, used for interrogation, are much larger than the thickness l of an individual layer within the cell (i.e., $\lambda \gg l$).[16] Carcione et al. calculated the ratio, R_{EM}, of wavelength λ and spatial period d_{EM}, at which the layered medium can be replaced with an equivalent or effective medium to be between 5 and 8 ($R_{EM} = \lambda/d_{EM}$).[17] It is well known that under the assumption of an effective medium, where the layered medium is replaced with a homogenous material of averaged properties of the constituent layers, deviations of up to 20% of the measured sound velocity from the expected sound velocity can be observed. This is known as Backus averaging.[16,18]

In the case of an isotropic elastic medium, the compressional (or pressure, or longitudinal) wave's sound velocity is

$$v_P = \sqrt{\frac{E(1-\nu)}{\rho(1-\nu-2\nu^2)}} \tag{1}$$

where E is the elastic modulus, ρ is the density, and ν is the Poisson's ratio of the bulk volume.[16,19] Similarly, the sound velocity of the shear (or transversal) wave is defined as

$$v_s = \sqrt{\frac{E}{2\rho(1+\nu)}} \tag{2}$$

In a simplified model considering a porous solid, Equation (1) is modified by a multiplication factor for the density, which accounts for the volume shares of the solid frame and the filled pores.[16] In the case of an evacuated porous network, this multiplication factor is $(1-\beta)$ with porosity β. In the case of a fluid or gas-filled porous volume, the density is replaced with $(1-\beta)\rho_s + \beta\rho_f$, where ρ_s and ρ_f denote the density of the solid frame and the density of the fluid, respectively. In several publications, a generalized equation for the sound velocity c in lithium-ion batteries has been defined as

$$c = \sqrt{E_{eff}/\rho} \tag{3}$$

where E_{eff} is the effective elastic modulus.[17,18]

It was shown that, depending on the measurement frequency, the layered structure of lithium-ion batteries might require the treatment of the sound propagation in individual layers to fully model the sound propagation. Recently, Huang et al. showed that the frequency-selective passing of sound waves through the layered structure of lithium-ion batteries can be modeled layer by layer and thus allows the reflected ultrasonic signal from the echoes generated at the current collector foil–electrode coating interface to be reconstructed.[19] They showed that in this case, the acoustic properties of the wet separator and electrode coating are similar and thus no significant reflections occur at the separator–electrode coating interface. Therefore, the layering of copper foil (anode current collector), anode coating, separator, cathode coating, and aluminum foil makes up a repetitive unit in which the criteria for resonance through constructive interference are fulfilled at certain frequencies.[19] Subsequently, the frequency spectrum of the signal in pulse-echo geometry shows peaks at multiples of this resonant frequency.

The propagation of sound waves in the individual battery material layers was discussed in several publications.[19,20] For the solid metal layers, that is, the current collector, sound propagation, as described in Equation (1) and (2), can be assumed. It was suggested to use Biot's theory to model the sound propagation in fluid-saturated porous media to describe the ultrasonic waves in lithium-ion batteries.[21] Huang et al., in contrast, suggested that the slurry model is better suited for the description of the propagation in the electrode coating due to the nature of the electrode, which consists of active material particles elastically linked by the binder and surrounded with electrolyte.[19] For the separator, they agree with Gold et al. that the sound propagation in the wet separator can be described with Biot's theory.[19,21]

**ADVANCED
SCIENCE NEWS**
www.advancedsciencenews.com

Energy Technology
Generation, Conversion, Storage, Distribution
www.entechnol.de

Biot's theory[22] considers the displacement of the porous solid frame and the fluid in its pores. Unlike in a bulk solid, an additional, second compressional wave mode exists alongside the shear wave mode. The main difference in the two compressional waves (the fast and the slow compressional waves) lies in the relative averaged displacement of fluid and solid. This tends to be in phase for the fast wave and out of phase for the slow wave. When the two phases are decoupled, which means that the solid frame that is much more rigid than the fluid, can oscillate at relatively high frequency; a more intuitive explanation can be provided. The fast wave corresponds to wave propagation in the solid frame, whereas the slow wave corresponds to the propagation in the fluid in the pores. Every solid has microstructure, for example, has a grain structure, and is made up of considerably large molecules or is host to heterogeneities such as pores and/or cracks. In the case of a lithium-ion battery, this microstructure is rather complex as it contains different layers, fibres (in the separator), and particles (both primary and secondary particles). Scattering of propagating elastic waves occurs when the wavelength becomes comparable to the characteristic size of the microstructure. Rayleigh scattering occurs when the wavelength λ is greater than the characteristic size d_{ms} of such structures, that is, $\lambda > d_{ms}$ (here ms denotes microstructure). Stochastic scattering occurs when $\lambda \approx d_{ms}$ and diffusion scattering occurs when $\lambda < d_{ms}$. When $\lambda >> d_{ms}$, wave scattering is negligible, and the porous medium behaves effectively as a homogeneous medium. Practically, wave scattering effects are negligible when $\lambda > 10d_{ms}$. This constitutes the upper limit of "very-high" frequencies and corresponds to a cutoff frequency of f_{scatt}

$$f_{scatt} \cong v_{PS}/10d_{ms} \qquad (4)$$

where v_{PS} stands for the velocity of the relevant pressure or shear wave in that medium, as stated above.

The objective of this article is the measurement of ultrasound velocity and spectral analysis of transmitted waves of different frequencies through different pouch cell stacks. The sound wave attenuation and time-dependent change can also be a threshold for unwet and wet regions in the pouch cell stack.

2. Measuring Acoustic Properties of Lithium-Ion Battery Cell Materials

2.1. Development of the Measurement Setup

The measurement setup was designed to ensure the application of homogeneous pressure to the samples while carrying out ultrasonic measurements in transmission geometry. A rigid frame was constructed for this purpose, which is displayed in **Figure 1**a. Within this frame, pressure plates are mounted on movable sleds, which allows a sample to be comfortably inserted and the transducers to be exchanged. Between the frame and the left sled, a load cell (LC) is mounted to measure the force built up within the frame by operating the jackscrew on the very right. Operating the jackscrew moves the spring-loaded plane (springs: SP) and builds up a force within the frame. As the force is the same on all elements, the resulting pressure on the sample can be calculated by the ratio of measured force and elevated surface of the sample.

In Figure 1b, a schematic representation of the setup is shown. The left pressure plate serves as a wedge (W). The term "wedge" is used in ultrasonic nondestructive testing synonymously with the term "delay line" and does not make implications about the shape. Therefore, wedges do not have to have surfaces at angle and can also be zero-degree wedges, as in this case. The thickness of the wedge is chosen to exceed the near-field length of the ultrasound in aluminum: the material of the wedge. Thereby, the sample is placed at a distance from the transducer that is considered the far field, in which the ultrasound pressure profile is uniform. In addition, the wedge serves as a delay line, ensuring that the sending waveform, which could be electrically transmitted from transmitter to receiver, does not overlay with the acoustic waveform in the received signal. The transmitting transducer (TR) is mounted on the back of the wedge, while the receiving transmitter (RE) is mounted within a cutout of the right pressure plate. The mount fixes the receiving transmitter horizontally and vertically in a plane parallel to the sample surface but allows it to move slightly in the axis perpendicular to the sample. A compressible silicone rubber foam layer is placed at the back of the transducer and acts as a spring. Without any load applied, the receiver stands out about 0.5 mm against the surrounding pressure plate. When the sample is gradually compressed by the pressure plates, the left pressure plate and the receiver are the first to make contact with the sample. By applying pressure, the silicone rubber layer on the back of the receiver is compressed until the right pressure plate is also fully in contact with the sample. This ensures a good coupling of the receiver while maintaining a homogeneous pressure on the sample.

The intensity at which ultrasound is transmitted at the interface between two media, for example, from a transducer into a sample, depends greatly on the difference in acoustic impedance at that interface. The effective exchange surface between the two media is also highly relevant as surface roughness can contribute greatly to reduced coupling. Therefore, a coupling agent is very often used to fill the voids at the junction of two media. For this purpose and depending on application, a variety of coupling agents can be considered. Common choices are water, gel, natural, or synthetic oil. Here, a natural, biological oil (rapeseed) was chosen due to its compatibility with the materials it was in contact with and the rather low requirements regarding the longevity of a stable contact.

In Figure 1c, the ultrasonic transmission and reflection events in a setup consisting of a transmitting transducer (TR), a wedge, a sample, and a receiving transducer (RE) are presented. For simplicity, the 1D case is depicted and only compressional (longitudinal waves) are considered. The y-scale depicts the travel distance within the different media of the setup. The x-scale represents the time of arrival at the opposing transducer (RE) in transmission mode or at the transmitting transducer (TR) when in pulse-echo mode. The ultrasonic wave is illustrated as an arrow at an angle, where the angle represents the sound velocity in the respective medium, for example, the steeper the angle, the higher the sound velocity. The first division into transmitted and reflected waves at the wedge–sample interface is represented by arrows with dashed lines. At each interface (transducer/wedge, wedge/sample, sample/transducer), the ultrasonic wave is partially reflected and transmitted. The ratio of the intensities of
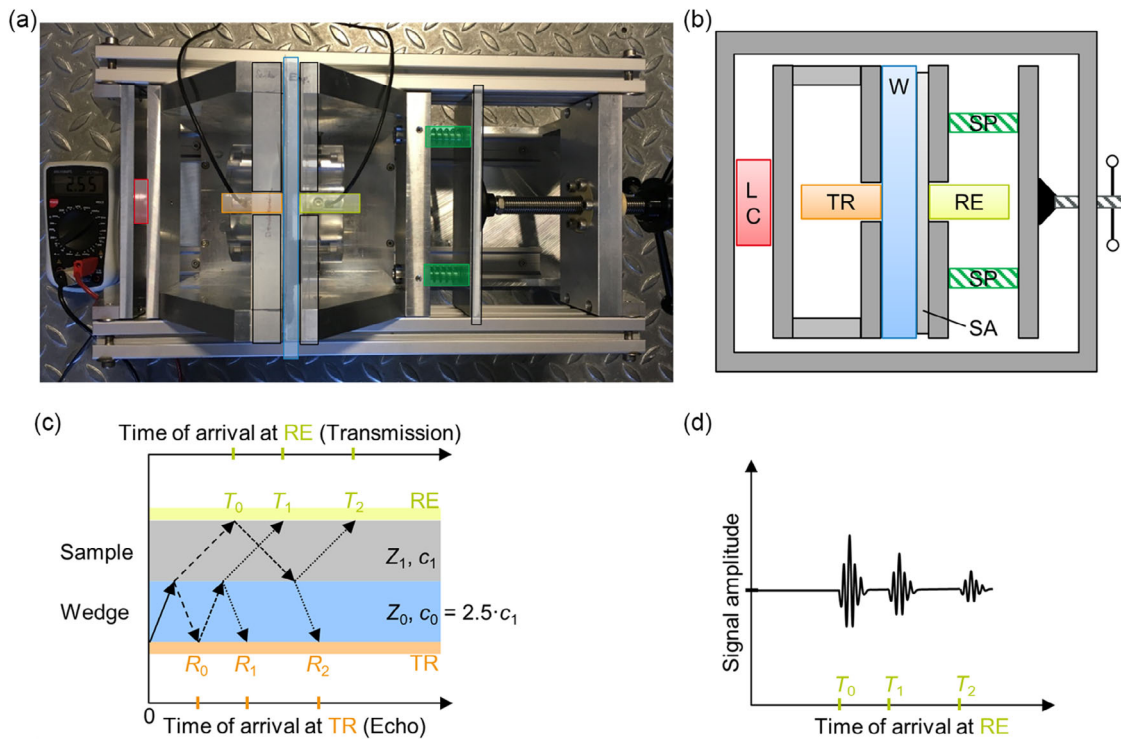
ADVANCED
SCIENCE NEWS
www.advancedsciencenews.com

Energy Technology
Generation, Conversion, Storage, Distribution
www.entechnol.de

Figure 1. a) Top-view image of the measurement setup. b) Schematic of the setup. Within a rigid frame, pressure plates are mounted on moveable sleds. A jackscrew allows two springs (SP, green) to be compressed and to build up pressure within the frame between the pressure plates (dark gray plates) and onto the sample (SA, light gray). The exerted pressure is measured by a load cell (LC). On the sending side, a wedge (W, light blue) serves as the pressure plate. Within the pressure plates, ultrasonic transducers are embedded and serve as transmitter (TR) and receiver (RE). c) 1D sketch of the reflection events leading to the exemplary, transmitted signal sketched in (d). In (c) the x-axis depicts the time of arrival at either of the transducers, while the y-scale depicts the travel distance of the sound wave. As the sound velocity c in the materials differ, the angle of the arrow, indicating the propagation of the sound wave, differs within the materials. Splitting of an incident wave into transmitted and reflected wave occurs at every interface with differences in acoustic impedance Z, which is represented by dashed arrows. With this representation, wave packages in a signal can be traced back to reflection at interfaces, yielding either sound velocity or travel distance, given that one of the formers is known a priori.

transmitted and reflected waves can be calculated based on the acoustic impedance Z_0 and Z_1 of the materials in contact at the interface. The intensity of the reflected wave can be calculated by

$$r = \frac{(Z_1 - Z_0)^2}{(Z_1 + Z_0)^2} \tag{5}$$

and the intensity of the transmitted wave by

$$t = 1 - r \tag{6}$$

A wave can be reflected multiple times. Therefore, the transmission signal, sketched in Figure 1d, contains wave packages resulting from direct transmission (T_0) and multiple reflections (T_1, T_2, ...). This leads to a reduction in intensity with every interface passed. At the receiver (RE), operating in through-transmission mode, only directly transmitted pulses and signals resulting from an even number of reflections can be observed. T_0 to T_2 represents the first three possible transmitted pulses, resulting from up to two reflections. At the transmitter (TR), operating in pulse-echo mode, only signals resulting from an odd number of reflections can be observed. R_0 to R_2 represents the first three possible signals resulting from up to three reflections.

2.2. Analysis Algorithm to Extract Ultrasonic Signal Properties

In **Figure 2**, an exemplary transmission signal is presented. The signal amplitude is plotted as a blue line versus the time after triggering the initial signal. The orange line represents the envelope of the signal, which is calculated via the Hilbert transform (see Experimental Section). The envelope allows a section of the signal, associated with the first acoustic wave package arriving at the receiver, as marked by the vertical dashed lines, to be estimated. For this first signal, the time of flight (ToF) is estimated with a threshold equal to 10% of the maximum amplitude of the signal. The ToF estimated by threshold ($\tau_{\text{th},0.10}$) and maximum of the envelope ($\tau_{\text{env,max}}$) are plotted as green and red dots, respectively. As pointed out in refs. [23–26], different ToF estimation techniques introduce varying levels of offset, also called bias error, and differ in achievable accuracy. For this contribution, several ToF estimation techniques have been tested and the threshold technique was selected due to its stability and reliability over the measurement frequency range and the variety of samples measured.

The spectral analysis of this signal is plotted separately in **Figure 3**. From the whole signal and the selection, the power spectral density (PSD) is calculated as the squared Fourier

**ADVANCED
SCIENCE NEWS**

www.advancedsciencenews.com

Energy Technology
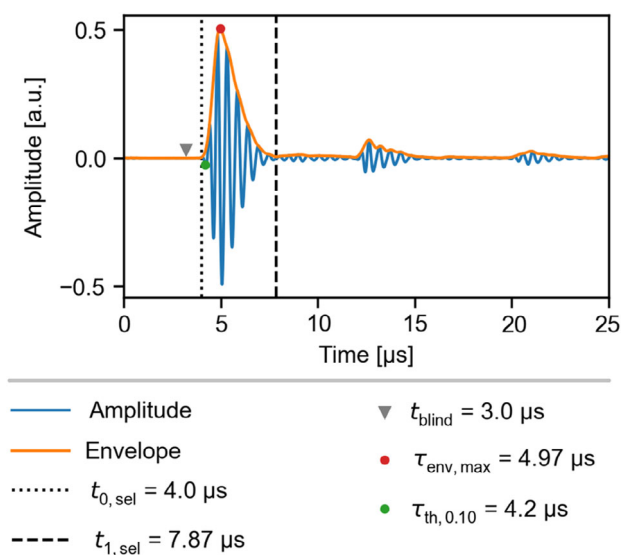Generation, Conversion, Storage, Distribution

www.entechnol.de

Figure 2. Transmission signal through the wedge at a measurement frequency of 2 MHz. The signal amplitude (blue line) is plotted along with the envelope (orange line). An inverted gray triangle marks the beginning of the search window, selected by the operator. The algorithm for the ToF estimation is set to be blind prior to that point t_{blind} by the operator. Red and green dots mark the ToF (symbol τ), estimated by the maximum of the envelope and by a threshold set to 10% of the maximum signal amplitude, respectively. Vertical dashed lines mark a selection of the signal containing the first-wave package.
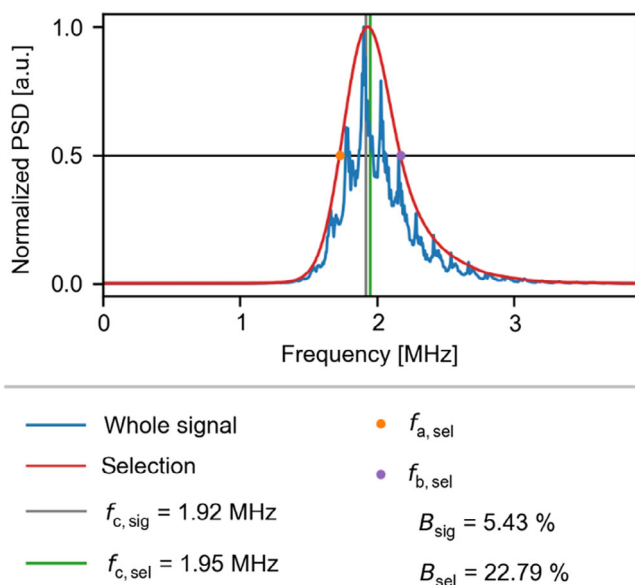

Figure 3. The PSD of the signal (blue line) and a selection of the signal (red line), as displayed in Figure 2, are normalized to the respective maximum. The PSD is calculated via the squared Fourier transform of the signal amplitude. The relative bandwidth B, given in the legend, is calculated from the ratio of absolute bandwidth and center frequency. As the PSD of the whole signal has a very narrow peak, the respective bandwidth is much smaller than that of the selection.

transform of the signal amplitude. The selected section of the signal refers to the first arrival at the receiving transducer and contains the first wave package of the signal. As pointed out in ref. [27], the whole signals contains arrivals resulting from a different number of reflections, leading to a different amplitude spectrum of the PSD due to their phase shift with respect to the first arrival. By normalizing the PSD and taking the intersection of the spectrum with the 0.5 line closest to its maximum, the frequencies f_a and f_b are estimated. The distance between f_a and f_b is called absolute bandwidth B_{abs}. The geometric mean of the two values is called center frequency f_c and is used along with the relative bandwidth $B_{rel} = (f_a - f_b)/f_c$ to characterize the spectral content of a signal or a section of the signal. As shown in Figure 3, the PSD of the whole signal and the selection deviate significantly in shape, one exhibiting many peaks and the other is very regularly bell shaped. Therefore, the relative bandwidth is also quite different. This shows that the whole signal contains frequency components in different ratios as it results from multiple reflections. To measure the direct transmission alone, the selection containing the first arrival is chosen for the quantification of the PSD. Therefore, the PSD of the selection is the basis for the analysis of the frequency of the transmitted signals throughout this work. The algorithm developed to estimate the signal properties is detailed in the Supporting Information.

2.3. Acoustic Properties of Lithium-Ion Battery Cell Materials

A large number of measurements were carried out on 70 individual samples. The following figures, unless otherwise stated, contain mean values with the standard deviation depicted as error bars. For each sample type, two to six samples were evaluated. As a reference, "baseline measurements" with two layers of the pouch foil as a sample were carried out. Interference patterns originating from closely spaced reflections were present in the resulting signals, which made a systematic ToF estimation not feasible. Therefore, reference "baseline measurements" with the aluminum wedge, but without a sample between the transmitting and receiving transducer, were chosen instead. To avoid similar effects within the measurement series, a minimum sample thickness of 0.5 mm was selected. The same aluminum wedge is used as a delay line in each measurement. As described above, ToF estimation techniques, such as the threshold technique, introduce an offset. In the reference "baseline measurements", a correction of the offset is required, which is described in the Supporting Information. The ToF in a sample alone is calculated by subtracting the ToF through the wedge from the ToF through the wedge and a sample. As both terms contain the offset, it is canceled out and no correction is required. **Table 1** lists the samples studied, along with the respective legend entries and color labels used in the graphs of this work. The construction of the samples is detailed in Experimental Section. Samples were either kept in a dry state and evacuated state or filled were with electrolyte and evacuated to 50 mbar before sealing. With this sample preparation strategy, the ultrasound propagation at the two extreme points during the wetting process, that is, fully dry and fully wet state, was investigated. The number of layers in each sample was chosen such that the sample thickness exceeds the thickness of the pouch foil by a factor of at least

ADVANCED
SCIENCE NEWS
www.advancedsciencenews.com

Energy Technology
Generation, Conversion, Storage, Distribution

www.entechnol.de

Table 1. List of samples with assigned legend entries and color labels.

Label	Content of the stack within the sample/description	Color	Number of dry samples	Number of wet samples
11× anode[a]	11 anode sheets		5	5
10× cathode[a]	10 cathode sheets		5	5
22× FS separator[b]	22 Freudenberg separator sheets		6	6
22× CG separator[b]	22 Celgard separator sheets		3	3
FS 1× cell stack[c]	Single cell stack with Freudenberg separator		6	5
CG 1× cell stack[c]	Single cell stack with Celgard separator		3	3
FS 10× cell stack[d]	Ten cell stacks Freudenberg separator		3	3
CG 10× cell stack[d]	Ten cell stacks Celgard separator		2	–
Aluminum wedge	Wedge, cut from a single piece of aluminum		–	–

All samples are sealed in a pouch bag. Dry samples: sealing at 50 mbar, wet samples: electrolyte dosing and sealing at 50 mbar. [a]Anode (A) and cathode (C) describes the double-sided electrode sheet; [b]Separator (S) describes a single sheet of the respective separator; [c]1× cell stack describes the layering of S|A|S|C|S sheets; [d]10× cell stack describes the layering of 10×(S|A|S|C)|S|A|S sheets.

two. To assess the ability of ultrasound to penetrate a battery cell comprising many cell stacks, samples with ten cell stacks were build. A stack is defined by the layer sequence of anode (A), separator (S), cathode (C), separator, represented as A|S|C|S. In this case, anode and cathode refer to a sheet of current collector foil, copper, or aluminum for A and C, respectively, coated on both sides with the respective negative or positive active material-containing electrode mass. The 10× cell stack samples contain 11 anode sheets, 10 cathode sheets, and 22 separator sheets, each with a layering sequence of 10×(S|A|S|C)|S|A|S. To estimate the propagation of ultrasound in each of the constituent, samples consisting of one type of layer were constructed with the same number of sheets. Initially, it was unclear if ultrasound could penetrate ten cell stack samples. Therefore, additional samples with a single cell stack, consisting of three separator sheets and one anode and one cathode sheet each (S|A|S|C|S), were constructed.

In **Figure 4**, the thickness and the density of the samples per sample type is depicted in the dry and wet states. The bars represent the mean values for all samples of a given type and the error bars represent the standard deviation. The thickness of the samples serves as an estimate for the travel distance of the ultrasonic waves from which the sound velocity is calculated

in combination with the ToF. The product of density and sound velocity is used to calculate the acoustic impedance of the samples. Since the dry samples were evacuated to a residual of 50 mbar pressure, the pore volume is filled with gas that merely contributes to the weight of the sample. The density of the samples increases due to filling the pore volume with electrolyte. The pouch bag has sufficient dead volume to host the excess electrolyte (40% more than the free pore volume). Therefore, the thickness increase of the samples is expected to arise solely from the swelling of the battery materials due to electrolyte soaking. The properties of the aluminum wedge are not displayed in the figure. Its thickness is 25.0 ± 0.1 mm and the density was estimated to be $2.65 \pm 0.01 \, \mathrm{g \, cm^{-3}}$.

As the ultrasound passes through the wedge and the sample under investigation, the amplitude of the signal is dampened at specific frequencies more significantly than at others, which depend on sample type. This leads to a change in the frequency distribution, as estimated by PSD, see Experimental Section.

Figure 5 displays the center frequency of the PSD, estimated from the selected section of the transmitted signal. The center frequency is plotted versus the measurement frequency, that is, the nominal frequency of the transmitting transducer. The selected section contains the first wave package and is determined as described in the Experimental Section. The results for the dry and electrolyte-filled samples are displayed in separate subplots. If passing through a particular sample volume did not selectively dampen specific frequency components of the signal, the respective data point would overlay the datapoint of the reference at the measurement frequency in question. In both subplots, the slope for the signals transmitted solely through the aluminum wedge, shown as a reference (black line), remains close to 1 until 4.6 MHz. Only the point at a measurement frequency of 9.5 MHz deviates and is shifted toward a higher frequency of 11.2 MHz. If the data point representing the measurements conducted on one type of sample is shifted toward higher frequency with respect to the reference, higher frequencies pass through the sample or are attenuated less compared to lower frequencies. If the data point is shifted toward lower frequencies, higher frequencies are attenuated selectively, for example, due to scattering at the microstructure. To illustrate this hypothesis, a sketch is provided in Figure S5, Supporting Information. Here, the amplitude modulation of the ultrasound wave by samples with different characteristics is presented in a semilogarithmic intensity spectrum (PSD). The samples, constructed from lithium-ion battery cell materials, are modeled as band stop filters. Depending on the position of the stop band, the center frequency of the PSD can be shifted to higher or lower frequencies, accompanied by an overall decrease in amplitude (intensity).

At the measurement frequencies of 1 and 2 MHz, all samples appear to selectively dampen higher frequencies or show little difference in the center frequency of the PSD in comparison with the reference. This trend continues at 4 MHz measurement frequency, except for two of the samples containing Celgard separator sheets, "22× CG separator" and "CG 1× cell stack." At higher frequencies, the observed trends do not continue.

For the "11× anode" samples, the center frequency remains around 4 MHz at measurement frequencies of 4 MHz and above, suggesting that those frequencies are selectively dampened when ultrasound passes through the sample volume. The resonance
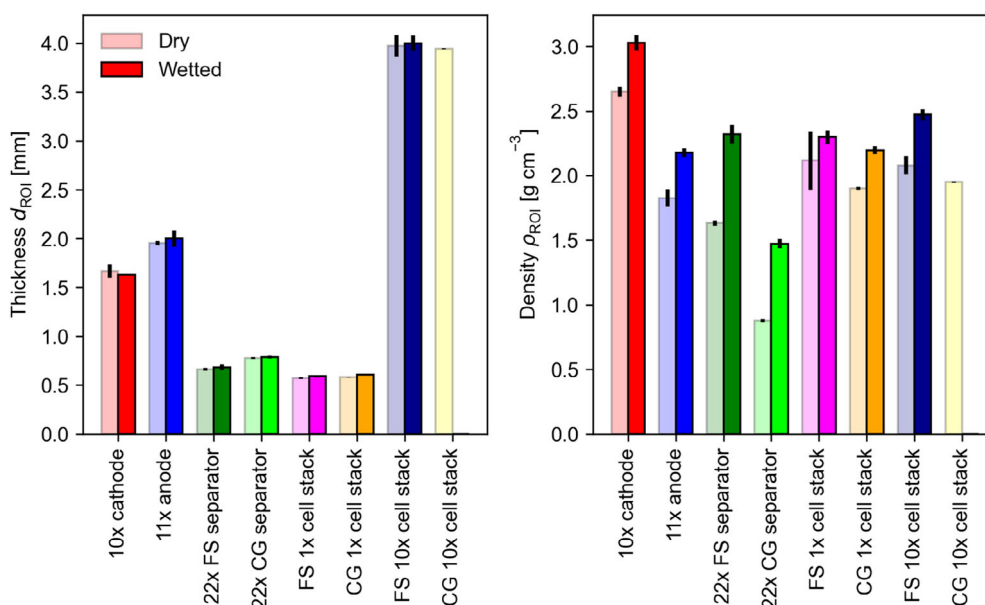
Figure 4. Thickness and density of the samples for each sample type in the dry and wet state. Content and number of layers per sample type are specified in Table 1. The density is calculated for the ROI, that is, the section of the sample that is representative for the volume through which the ultrasound travels. The density calculation is detailed in the Supporting Information.
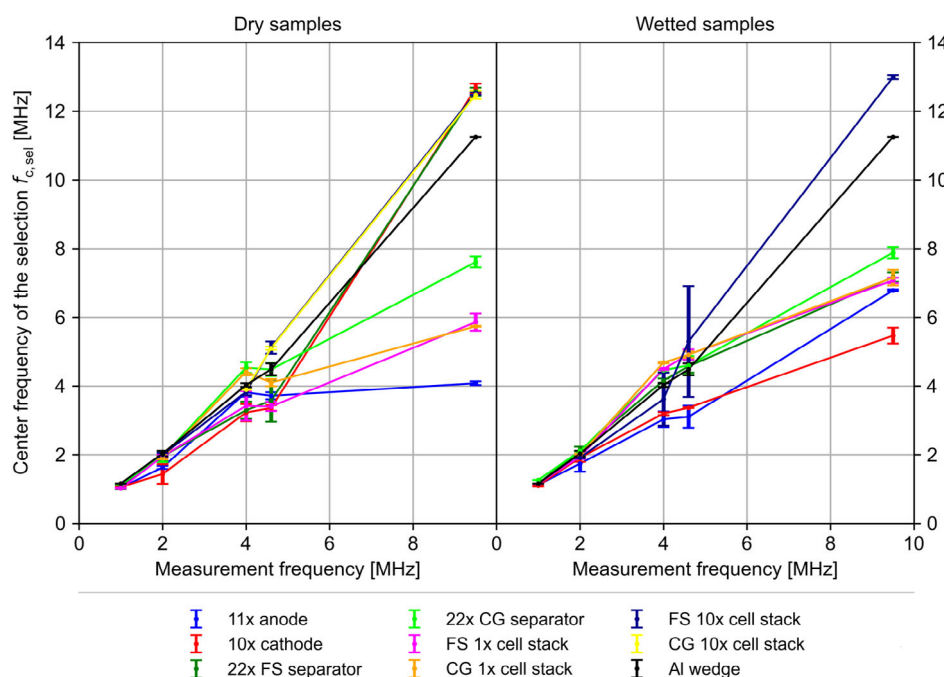

Figure 5. Center frequency $f_{c,sel}$ of the PSD of a selected section of the transmission signal, plotted versus the measurement frequency of the transmitting transducer. This selection refers to the first-wave package. The mean values for different samples of each type are plotted with the standard deviation as error bars. The solid line connecting the data points serves as a guide for the eye.

model, established by Huang et al.,[19] could provide an explanation for the observed frequency modulation at these measurement frequencies. They observed a resonance frequency similar to that observed here for cells with very similar dimensions and properties (refer to Supporting Information). The

samples containing ten cell stacks as defined above ("CG 10× cell stack" and "FS 10× cell stack"), as well as the "10× cathode" and "22× FS separator," show a center frequency of about 12.5–12.7 MHz at a measurement frequency of 9.5 MHz. For these measurements, an exemplarily comparison

**ADVANCED
SCIENCE NEWS**
www.advancedsciencenews.com

Energy Technology
Generation, Conversion, Storage, Distribution
www.entechnol.de

of the intensity spectra (PSD) with the reference is included in the Supporting Information. In Figure S6, Supporting Information, the intensity peak is reduced by several orders of magnitude while being shifted to higher frequencies, with respect to the reference. The remaining samples are located between "11× anode" at about 4 MHz and the reference at 11.5 MHz. The distance to the next lower datapoint is about 4 MHz. To enable a better understanding of the results, the frequency range between 4 and 9.5 MHz should be investigated.

For the wet samples, a similarly heterogeneous picture arises. Here the samples containing electrode sheets alone ("11× anode" and "10 cathode") show a shift toward lower frequencies. At measurement frequencies up to 4.6 MHz, the center frequencies of the remaining samples are shifted to higher frequencies with respect to the reference. At measurement frequency of 9.5 MHz, all other samples are located between the electrodes and the reference, as expected. Only the "FS 10× cell stack" sample deviates significantly. These samples show very similar behavior for the wet and dry state. This suggests that the respective samples undergo increased gassing or may have taken in air through a defect in the pouch seal over the course of the measurement series, which starts at 2 MHz, followed by 9.5 MHz, and finishes with 4 and 4.6 MHz.

Frequency-selective dampening can originate from several effects. Scattering occurs at every interface within the path of the ultrasonic wave. This includes the boundaries between wedge, sample, and transducer as well as within the sample. Structures within the samples that might scatter sound might be particles, for example, active material particles or ceramic fillers, fibers or layers, for example, the current collector foil and the coating of the electrodes. Depending on wavelength and acoustic

impedance, the sound can be scattered at these structures. These two acoustic properties are calculated from the sound velocity.

Figure 6 shows the sound velocity in different sample types in the dry and wet state. The sound velocity $c = d_{ROI}/\tau$ is calculated from the ToF τ of the first wave package, transmitted through the sample and the thickness d_{ROI} of the sample, measured in the region of interest (ROI), which contains the stacked layers of battery materials. For the results, presented here, the ToF estimated by the threshold technique, where applying 10% of the maximum amplitude of the signal as the threshold, is used. As the ultrasound passes through the wedge and the sample, a separate "baseline measurement" without a sample is performed. The ToF through the wedge is subtracted from the ToF through wedge and sample, which yields the ToF through the sample alone. The "baseline measurement" is plotted as a reference in Figure 6 (black data points). A small increase of sound velocity in aluminum with frequency is observed. This common effect is called dispersion and occurs in most media.[28]

For the dry samples, the sound velocity in different types of samples shows a rather uniform picture, with the exception of the data points for the "22× FS separator" and the "10× cathode" at a measurement frequency of 9.5 MHz. Those two data points are considered outliers as they occur at a sound velocity that is from a physical perspective too low. These two datapoints also show a shift in center frequency with respect to the reference. An increase in sound velocity is expected with increasing measurement frequency. Nevertheless, the recorded transmission signals, which have a low signal-to-noise ratio, did not allow an earlier arrival to be identified, which would have resulted in a sound velocity reasonable for that associated with sound propagation in a solid.
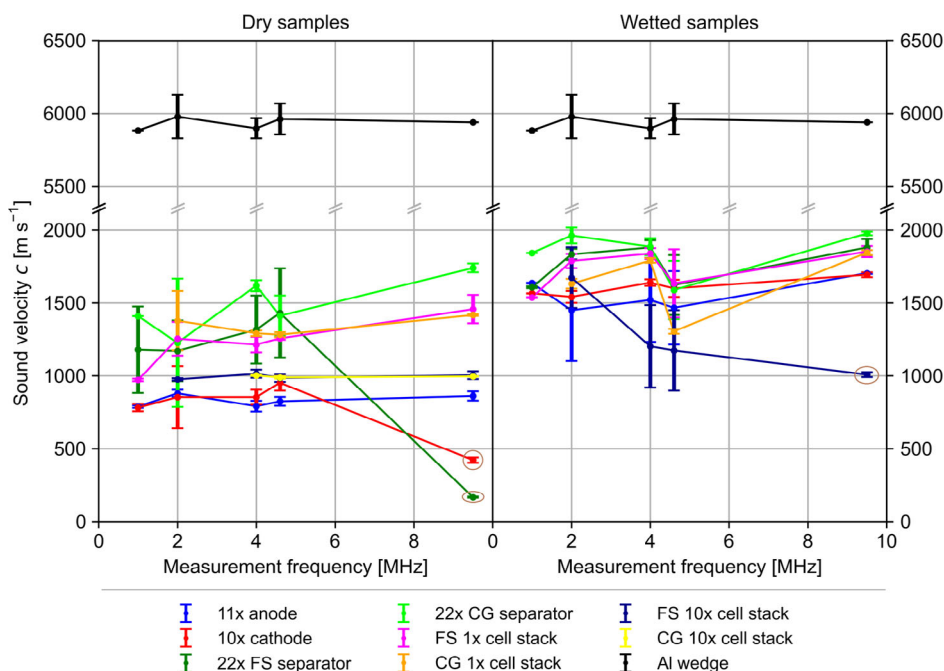

Figure 6. Sound velocity, c, in the dry and wet samples, calculated from the thickness of the sample and the first detectable wave package within the transmission signal, plotted against measurement frequency. The mean values for different samples of each type are plotted with the standard deviation as error bars. Outliers are marked with a light-brown ellipse.

**ADVANCED
SCIENCE NEWS**
www.advancedsciencenews.com

Energy Technology
Generation, Conversion, Storage, Distribution

www.entechnol.de

The lowest sound velocity is measured in the electrodes, with exception of the outliers. These consist primarily of the active material particles coated onto thin metal foils. The mechanical properties of the electrodes are known to be dominated by the comparably soft binder since the application of external pressure does not significantly compress the active material particles but rather shifts their position within the elastic binder framework.[29,30] Therefore, the overall elastic modulus of the electrode is dominated by the binder properties and not by the properties of the component with the highest mass share, that is, the active material particles. Subsequently, the overall elastic modulus of the electrode lies orders of magnitude lower than the elastic modulus of the active material particles.[29] As the sound velocity within a material is proportional to the square root of its elastic modulus divided by its density, the observed result is expected.

As the sound velocity is proportional to the square of elastic modulus divided by density, an increase in sound velocity with decreasing density and vice versa is expected. Therefore, the decreasing trend of the density of the first four dry sample types (electrodes and separators) in Figure 4 correlates well with the order of sound velocity of these sample types in Figure 6.

The other types of samples are located in between the electrodes and separators. The samples with one cell stack containing three layers of separator and two electrode layers have higher values than the sample types with ten cell stacks. With one cell stack, the ratio of separator layers to electrode layers is 3:2 = 1.5. In contrast, the samples with ten cell stacks have a ratio of separator layers to electrode layers that is close to one (22:21). Assuming a linear mixing model, a ratio of 1.5 yields a sound velocity closer to that of the separator samples, while a sound velocity closer to that of the electrodes is found with a ratio closer to one.

With the wetting of the materials, differences in behavior can be expected, since the wetting increases the density of the samples due to the filling of the pores. Given that the various sample types have different porosities, the change in density depends on the sample type, as can be seen in Figure 4. Additionally, it is known that the elastic properties of electrodes change due to wetting with electrolyte.[31,32] Nevertheless, the elastic modulus of all battery materials in wet state is not easily accessible in the literature. Depending on the binder, the electrodes can soften significantly,[33,34] particularly with PVDF, which is known to absorb large quantities of solvent.[32,35,36] Thus, both the change in the elastic modulus and the density will affect the sound velocity due to wetting. The results in Figure 6 show that the order of sample types roughly stays the same after wetting, with exception of the sample "FS 10× cell stack." In this case, a similar sound velocity as the comparable dry samples has been determined, suggesting that the wet samples might still contain a gas volume in the ultrasonic pathway. The electrodes have the lowest sound velocity, while two separator sample types have the highest and the samples containing cell stacks are in between. The electrodes (C and A) change places, which might be a result of different degrees of softening of the different binders (PVDF vs. a mixture of SBR and CMC). Since the porosity of the electrodes differs only by about 6%, as shown in Table S1, Supporting Information, the softening of the binder probably is the more dominant effect.

Overall, the sound velocity increases by a factor of up to two in the different battery materials from the dry to the wet state. This can be considered a rather large effect and thus is an appropriate figure of merit to be used as a measure for the degree of wetting.

As explained in Section 2.1, the acoustic impedance of the materials to be investigated plays a decisive role for the adaptation of ultrasonic transducers and wedges. The acoustic impedance is also relevant for modeling the reflection and scattering processes within a sample. To act as a stochastic scatterer, an object or structure within a sample has to have a size in the order of magnitude of the wavelength and its acoustic impedance must be significantly different from that of the surrounding material. **Figure 7** shows the acoustic impedance calculated by multiplying the density ρ and the sound velocity c of the samples according to $Z = \rho \cdot c$. Since the sound velocity and the density increases strongly due to electrolyte filling, a corresponding increase in the acoustic impedance is expected and observed here. The behavior of the samples, containing a single-cell stack, is particularly relevant for the subsequent application in battery cell testing. The acoustic impedance of the single-cell stack doubles from $\approx 2\,\mathrm{MPa\,s\,m^{-1}}$ to $\approx 4\,\mathrm{MPa\,s\,m^{-1}}$ (MRayl). Therefore, the acoustic impedance of the wedge and the ultrasonic transducer should be adjusted to 3 MRayl in order to limit the reflected intensity at the interface to 15% (see Equation (6)) for both sample extremes, that is, the dry and wet states, along with everything in between.

The properties derived from the signal center frequency f_c of the PSD and sound velocity c in the samples allow calculating the wavelength $\lambda = c/f_c$. The wavelength is plotted against measurement frequency in **Figure 8**, with the results for dry and wet samples displayed in separate subplots. With a constant center frequency, the wavelength within the wet sample will increase due to the increase of sound velocity. Since the sound velocity in the dry samples "11× anode" and "22× FS separator" was around $400\,\mathrm{m\,s^{-1}}$ and the center frequency of these two along with the "CG 10× cell stack" samples was exceptionally high, at about 12.6 MHz. These three have wavelengths below 0.1 mm. Similarly, the measurements on the wet samples of type "FS 10× cell stack" yield a much lower wavelength than the other sample types. Those four should be considered as outliers for previously discussed reasons.

For both, dry and wet samples, a general trend can be observed. The wavelength decreases with measurement frequency, as wavelength is proportional to $1/f_c$. As seen before, center frequency f_c increases with measurement frequency. In the dry state, the wavelength varies between 1.25 and 0.2 mm, with the exception of the outliers described. In the wetted state, the wavelength varies between 1.46 and 0.25 mm in the frequency range measured. As described in the Introduction, interaction between the ultrasound waves and the internal structure occurs if the size of the structures is on the order of magnitude of the wavelength and results in scattering and reflections. Therefore, calculating the wavelength at a given measurement frequency allows the interaction of the ultrasound wave with structures within the samples to be estimated. These considerations can be used to identify measurement frequencies useful for accessing averaged properties at comparably large wavelengths or for resolving the microstructure of the battery materials.

For all sample types, the average size of the microstructure (particles, fibers, cracks) is well below 1/10 of the average
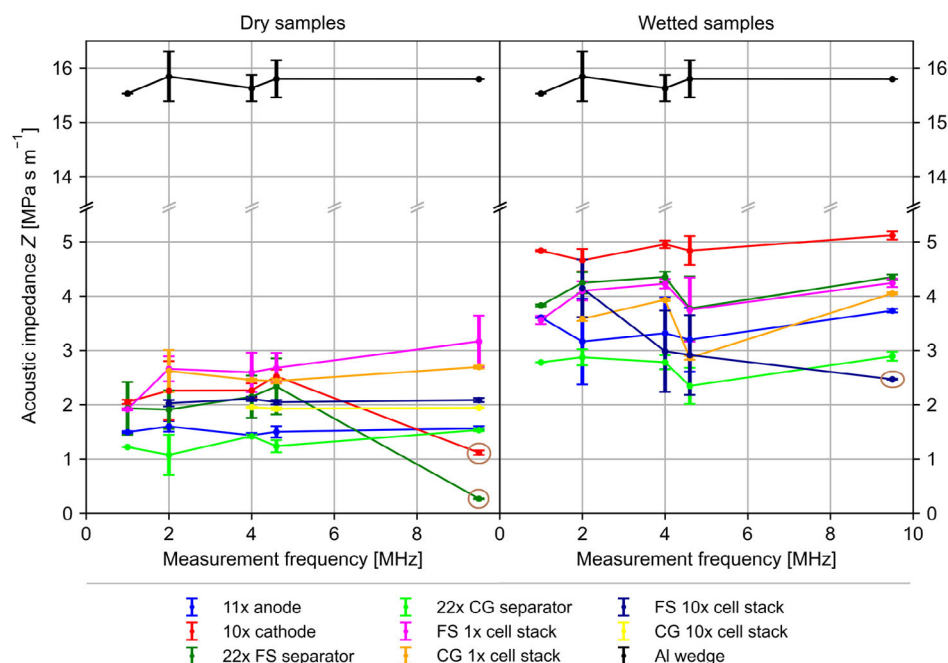
Figure 7. Acoustic impedance of the samples in the dry and wet state, plotted against measurement frequency. Acoustic impedance is calculated from the product of density and sound velocity. The mean values for different samples of each type are plotted with the standard deviation as error bars. Outliers are marked with a light-brown ellipse.
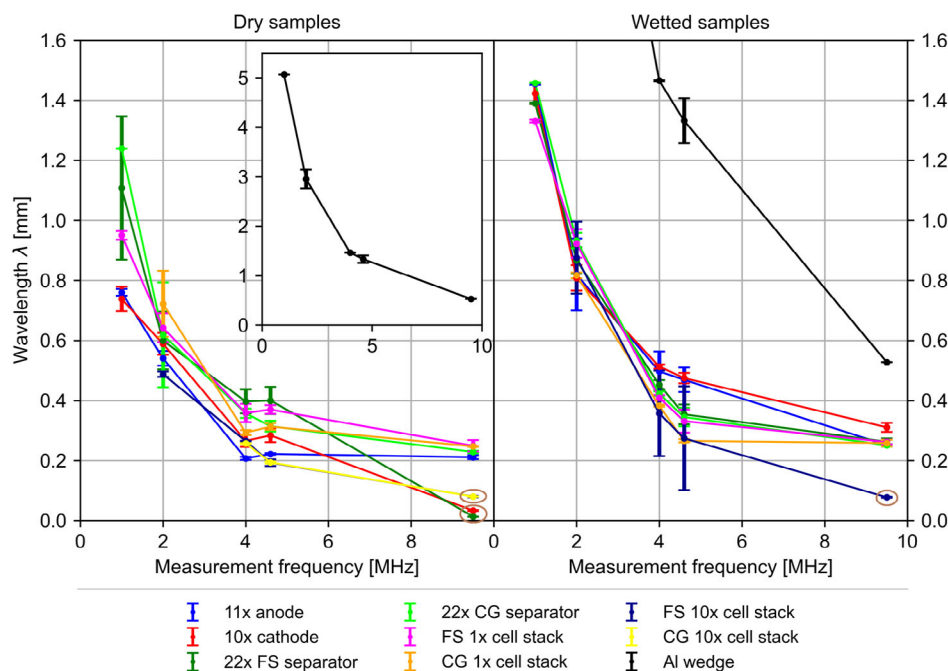
Figure 8. Wavelength plotted versus the measurement frequency. The wavelength is calculated from the quotient of the sound velocity and center frequency of the PSD of the selected signal section, which is associated with the first-wave package. Results for dry and wet samples are plotted separately. The inset shows the result for the aluminum wedge, which serves as a reference. The mean values for different samples of each type are plotted with the standard deviation as error bars. Outliers are marked with a light-brown ellipse.

wavelength in the frequency range presented, with exception of the outliers resulting from particularly low sound velocities or particularly high center frequencies. The periodicity of the stacked samples should also be considered. In particular, the spacing between two adjacent metallic layers is relevant, as these structures generally exhibit a jump in acoustic impedance,

**ADVANCED
SCIENCE NEWS**
www.advancedsciencenews.com

Energy Technology
Generation, Conversion, Storage, Distribution

www.entechnol.de

compared to the more porous components. The various material specifications are given in the Supplementary Information. The periodicity in samples with layers of electrodes alone can be calculated as 100 and 140 µm, for "10× cathode" and "11× anode," respectively. In samples containing full battery cell stacks, it is 137–146 µm for the Freudenberg and Celgard separators, respectively. Therefore, the minimum ratio of the wavelength to the periodicity of a medium of 5–8, as described by Carcione et al.,[37] is not given for all measurement frequencies. Particularly above 2 MHz, where the wavelength lies mostly below 1 mm, theoretical considerations should involve a treatment of the medium layer by layer instead of applying effective medium theory.

Freudenberg and Celgard separators were measured to be 17 and 26 µm thick, respectively (see Table S1, Supporting Information). In the absence of a metallic central layer, as in the electrodes, their acoustic properties are assumed to be uniform throughout their thickness with respect to the measurement frequencies utilized. Therefore, no periodic jump in acoustic impedance is expected within samples containing a stack of separator layers alone.

3. Conclusion

In this contribution, the development of a setup and evaluation routine for the acoustic properties of lithium-ion batteries has been showcased. An algorithm was introduced to estimate the ToF and thereby the sound velocity, of the first ultrasonic wave package in transmission signals. With a spectral analysis of the signals, the wavelength of the transmitted waves in various battery materials could be calculated and thus interactions of sound waves with the microstructure could be estimated. By deriving the density of the samples from their weight and volume, the acoustic impedance of the battery materials became accessible. To the best of the authors knowledge, this is the first time that the sound propagation in different battery materials was studied separately and that a range of measurement frequencies (over an order of magnitude) was used for interrogation.

Most importantly, this work demonstrates that a huge change in the sound velocity of up to 100% is observed when the porous structure of a lithium-ion battery is filled with electrolyte. This provides an additional criterion, beyond the transmitted amplitude as shown by Deng et al.,[15] to evaluate the degree of wetting. As the ultrasonic interrogation of battery cells develops at a rapid pace, the deployment of the technique as an inline monitoring or testing solution in battery cell production is emerging. In a broader context, ultrasound may be applied as a monitoring, imaging, and evaluation tool for production processes, as well as during battery cell application and in end-of-life scenarios.

The acoustic impedance is an important parameter for the design and fitting of ultrasonic transducers to a testing task, as the achievable signal quality depends largely on the matching of the acoustic impedance of the transducer and device under test. Adapting the transducers will enable the spectroscopic interrogation of battery cells in a through-transmission configuration and thus fill the gaps between the measurement frequencies used in this work.

4. Experimental Section

Preparation of the Samples: The samples under investigation were a custom-format pouch cell type. For this format, the components of the stack were cut to 157 × 100, 155 × 98, and 161 × 104 mm² for anode, cathode, and separator, respectively. The stacks were assembled semiautomatically with an in-house-developed Z-folder in laboratory atmosphere. Subsequently, the stacks were dried under vacuum at 80 °C for at least 8 h and transferred to an inert atmosphere. Depending on sample type, the stack was fit with current collector tabs (stacks with functional compartments only) and enclosed in a pouch bag. Electrolyte dosing under vacuum, at a residual pressure of 50 mbar, and subsequent sealing was performed in a vacuum filling and sealing machine by Harro Höflinger. Sealing of dry samples was performed in a Multivac C100. The electrolyte quantity to be dosed was determined according to Günther et al. [cite] as 1.4 times the free pore volume within the sample.

Electrodes were purchased from Custom Cells Itzehoe GmbH on rolls, already calendared. Electrodes were cut from these rolls with a rotational punching device, supplied by Harro Höflinger. Anodes were coated on 10 µm-thick copper foil with a mass loading of 9.2 mg cm⁻², corresponding to 3.2 mAh cm⁻², on each side. The electrode coating contained by weight 94% SMGA5 graphite, 2% carboxymethyl cellulose (CMC), 3% styrene-butadiene rubber (SBR) and 1% C65 carbon black. Cathodes were coated on 15 µm-thick aluminum foil with a mass loading of 17.3 mg cm⁻² and 2.9 mAh cm⁻², on each side. The coating consisted of 95.5% $LiNi_{0.6}Mn_{0.2}Co_{0.2}O_2$ (NMC622, BASF SE), 3% conductive additive, and 1% polyvinylidene difluoride (PVDF), by weight.

Two separators were investigated, the CG2325 (Celgard LLC), a 25 µm-thick, microporous trilayer polypropylene(PP)/polyethylene(PE)/PP separator CG2325 with a typical porosity of 39%, and the FS3011 (Freudenberg & Co. KG), a 22 µm-thick, nonwoven, wet-laid PE separator, impregnated with ceramic particles and a typical porosity of 59%. The electrolyte was LP572 (Targray technology international Inc), consisting of 1M solution of $LiPF_6$ in a mixture of ethylene carbonate (EC) and ethyl methyl carbonate (EMC) in a weight ratio of 3:7 with 2 wt% of vinylene carbonate (VC). The pouch foil D-EL40H was purchased from Kanematsu Corporation and current collector tabs were from Sumitomo Metal Mining Co Ltd.

Characterization of the Samples: Samples were weighed after assembly, using a Satorius Cubis MCE2203S-2S00-R laboratory balance. The lateral dimensions of the samples were determined with a precision ruler and the thickness was measured with a S_Dial Nano dial indicator (Sylvac SA). The thickness of the samples was measured at several points in the ROI, that is, the volume containing the stack and the pouch foil. Measurements were averaged per sample and within a group of the same sample type. The density of the ROI was then calculated from the weight and the volume, as detailed in the Supporting Information. The porosity of the electrodes was determined by Hg porosimetry, which is a standard method and was carried out similarly to that reported in other studies.[38,39]

Mechanical Pressure Setup and Cell Bracing: The setup providing adjustable mechanical pressure during ultrasonic transmission measurements was designed and constructed in house to fit the samples investigated. The basic structure of the rigid frame was constructed from aluminum bars and plates. The load cell (KM38-2kN ME-Meßsysteme GmbH) was used to measure the applied clamping force. The two springs (type 13 330, Sodemann Industrifjedre A/S) were used to provide almost constant pressure.

Ultrasound Measurements: Ultrasonic signals were excited and recorded using a PCUS pro Single, manufactured by Fraunhofer IKTS, Dresden, Germany. The transmitting transducer was excited with a needle pulse, tuned in length to match half of a period associated with the nominal measurement frequency of the transducer in use. For example, the length of the pulse was calculated by $t = (2f_0)^{-1}$, with f_0 being the nominal measurement frequency of the transducer.

The displayed and/or processed signals, which were the result of 32 averaged single measurements, were recorded at 100 MHz and spaced 40 µs apart. The envelope of the signal was calculated via the Hilbert transform and used for the semiautomatic selection of the first-wave package.

**ADVANCED
SCIENCE NEWS**

www.advancedsciencenews.com

Energy Technology
Generation, Conversion, Storage, Distribution

www.entechnol.de

Measurements were carried out by hand. Samples were placed in between the pressure plates; the pressure was adjusted to the desired level of 0.1 MPa and parameters of the signal recording were adjusted to reach 60% of the maximum amplitude level. Depending on the signal attenuation by the sample, an analogue 40 dB preamplification and a continuous digital amplification of up to 80 dB were applied. Further processed measurement datasets were a result of at least 32, and up to 128, depending on signal–to-noise ratio, averaged single measurements, recorded 40 ms apart. Different measurement frequencies required the exchange of the transducers. Transducer pairs with nominal measurement frequencies of 1, 2, 4, 4.6, and 9.5 MHz (United NDT GmbH) were used.

Supporting Information

Supporting Information is available from the Wiley Online Library or from the author.

Conflict of Interest

The authors declare no conflict of interest.

Data Availability Statement

The data that support the findings of this study are available from the corresponding author upon reasonable request.

[1] Y. Liu, R. Zhang, J. Wang, Y. Wang, *iScience* **2021**, *24*, 102332.
[2] J. B. Habedank, F. J. Günter, N. Billot, R. Gilles, T. Neuwirth, G. Reinhart, M. F. Zaeh, *Int. J. Adv. Manuf. Technol.* **2019**, *102*, 2769.
[3] T. Knoche, G. Reinhart, *Appl. Mech. Mater.* **2015**, *794*, 11.
[4] F. J. Günter, C. Burgstaller, F. Konwitschny, G. Reinhart, *J. Electrochem. Soc.* **2019**, *166*, A1709.
[5] T. Knoche, V. Zinth, M. Schulz, J. Schnell, R. Gilles, G. Reinhart, *J. Power Sources* **2016**, *331*, 267.
[6] M. Lanz, E. Lehmann, R. Imhof, I. Exnar, P. Novák, *J. Power Sources* **2001**, *101*, 177.
[7] W. J. Weydanz, H. Reisenweber, A. Gottschalk, M. Schulz, T. Knoche, G. Reinhart, M. Masuch, J. Franke, R. Gilles, *J. Power Sources* **2018**, *380*, 126.
[8] T. B. Reddy, *Linden's Handbook of Batteries. Set 2*, McGraw-Hill Professional; McGraw-Hill [distributor], New York, London **2010**.
[9] M. Yoshio, *Lithium-Ion Batteries*, Springer, Dordrecht **2010**.
[10] A. Schilling, P. Gümbel, M. Möller, F. Kalkan, F. Dietrich, K. Dröder, *J. Electrochem. Soc.* **2018**, *166*, A5163.
[11] A. Schilling, S. Wiemers-Meyer, V. Winkler, S. Nowak, B. Hoppe, H. H. Heimes, K. Dröder, M. Winter, *Energy Technol.* **2020**, *8*, 1900078.
[12] F. J. Günter, J. B. Habedank, D. Schreiner, T. Neuwirth, R. Gilles, G. Reinhart, *J. Electrochem. Soc.* **2018**, *165*, A3249.
[13] N. Kaden, N. Schlüter, R. Leithoff, S. Savas, S. Grundmeier, K. Dröder, *Processes* **2021**, *9*, 1851.
[14] L. Pitta Bauermann, L. V. Mesquita, C. Bischoff, M. Drews, O. Fitz, A. Heuer, D. Biro, *J. Power Sources Adv.* **2020**, *6*, 100035.
[15] Z. Deng, Z. Huang, Y. Shen, Y. Huang, H. Ding, A. Luscombe, M. Johnson, J. E. Harlow, R. Gauthier, J. R. Dahn, *Joule* **2020**, *4*, 2017.
[16] J. Jocker, D. Smeulders, *Ultrasonics* **2009**, *49*, 319.
[17] W. Chang, R. Mohr, A. Kim, A. Raj, G. Davies, K. Denner, J. H. Park, D. Steingart, *J. Mater. Chem. A* **2020**, *8*, 16624.
[18] K. W. Knehr, T. Hodson, C. Bommier, G. Davies, A. Kim, D. A. Steingart, *Joule* **2018**, *2*, 1146.
[19] M. Huang, N. Kirkaldy, Y. Zhao, Y. Patel, F. Cegla, B. Lan, *J. Energy Storage* **2022**, *50*, 104585.
[20] A. G. Hsieh, S. Bhadra, P. J. Gjeltema, D. A. Steingart, *Meet. Abstr.* **2015**, *MA2015-02*, 85.
[21] L. Gold, T. Bach, W. Virsik, A. Schmitt, J. Müller, T. E. Staab, G. Sextl, *J. Power Sources* **2017**, *343*, 536.
[22] M. A. Biot, *J. Acoust. Soc. Am.* **1956**, *28*, 168.
[23] L. Espinosa, J. Bacca, F. Prieto, P. Lasaygues, L. Brancheriau, *Acta Acust. United Acust.* **2018**, *104*, 429.
[24] L. Svilainis, in *52nd Annual Conf. of the British Institute of Non-Destructive Testing 2013 (NDT 2013)*, Telford, UK, September **2013**.
[25] J. C. Jackson, R. Summan, G. I. Dobie, S. M. Whiteley, S. G. Pierce, G. Hayward, *IEEE Trans. Ultrason. Ferroelectr. Freq. Control* **2013**, *60*, 343.
[26] B. Barshan, *Meas. Sci. Technol.* **2000**, *11*, 45.
[27] T. Pialucha, C. Guyott, P. Cawley, *Ultrasonics* **1989**, *27*, 270.
[28] J. Krautkrämer, H. Krautkrämer, *Werkstoffprüfung mit Ultraschall*, Springer Berlin Heidelberg; Imprint; Springer, Berlin, Heidelberg **1986**.
[29] D. Sauerteig, N. Hanselmann, A. Arzberger, H. Reinshagen, S. Ivanov, A. Bund, *J. Power Sources* **2018**, *378*, 235.
[30] D. Sauerteig, *Implementierung und Parametrierung eines physikalischen Simulationsmodells einer Lithium-Ionen Zelle zur Analyse elektrochemisch-mechanischer Wechselwirkungen*, Universitätsbibliothek, Ilmenau **2018**.
[31] Y. Wang, Q. Zhang, D. Li, J. Hu, J. Xu, D. Dang, X. Xiao, Y.-T. Cheng, *Adv. Energy Mater.* **2018**, *8*, 1702578.
[32] L. S. de Vasconcelos, N. Sharma, R. Xu, K. Zhao, *Exp. Mech.* **2019**, *59*, 337.
[33] Z. Chen, L. Christensen, J. R. Dahn, *J. Appl. Polym. Sci.* **2004**, *91*, 2958.
[34] T. M. Miller, L. Zhao, A. B. Brennan, *J. Appl. Polym. Sci.* **1998**, *68*, 947.
[35] C. Wendt, P. Niehoff, M. Winter, F. M. Schappacher, *J. Power Sources* **2018**, *391*, 80.
[36] A. Magasinski, B. Zdyrko, I. Kovalenko, B. Hertzberg, R. Burtovyy, C. F. Huebner, T. F. Fuller, I. Luzinov, G. Yushin, *ACS Appl. Mater. Interfaces* **2010**, *2*, 3004.
[37] J. M. Carcione, D. Kosloff, A. Behle, *Geophysics* **1991**, *56*, 245.
[38] S. Radloff, L. S. Kremer, A. Hoffmann, M. Wohlfahrt-Mehrens, *Mater. Today Commun.* **2021**, *28*, 102549.
[39] L. Froboese, P. Titscher, B. Westphal, W. Haselrieder, A. Kwade, *Mater. Charact.* **2017**, *133*, 102.